
RECURRENT NEURAL NETWORK-COUPLED SPAD TCSPC SYSTEM FOR REAL-TIME FLUORESCENCE LIFETIME IMAGING

A PREPRINT

Yang Lin Paul Mos Andrei Ardelean Claudio Bruschini Edoardo Charbon

Advanced Quantum Architecture Laboratory

École polytechnique fédérale de Lausanne

Neuchâtel, 2002, Switzerland

{yang.lin, paul.mos, andrei.ardelean, claudio.bruschini, edoardo.charbon}@epfl.ch

June 28, 2023

ABSTRACT

Fluorescence lifetime imaging (FLI) has been receiving increased attention in recent years as a powerful imaging technique in biological and medical research. However, existing FLI systems often suffer from a tradeoff between processing speed, accuracy, and robustness. In this paper, we propose a SPAD TCSPC system coupled to a recurrent neural network (RNN) for FLI that accurately estimates on the fly fluorescence lifetime directly from raw timestamps instead of histograms, which drastically reduces the data transfer rate and hardware resource utilization. We train two variants of the RNN on a synthetic dataset and compare the results to those obtained using the center-of-mass method (CMM) and least squares fitting (LS fitting) methods. The results demonstrate that two RNN variants, gated recurrent unit (GRU) and long short-term memory (LSTM), are comparable to CMM and LS fitting in terms of accuracy and outperform CMM and LS fitting by a large margin in the presence of background noise. We also look at the Cramer-Rao lower bound and detailed analysis showed that the RNN models are close to the theoretical optima. The analysis of experimental data shows that our model, which is purely trained on synthetic datasets, works well on real-world data. We build a FLI microscope setup for evaluation based on Piccolo, a 32×32 SPAD sensor developed in our lab. Four quantized GRU cores, capable of processing up to 4 million photons per second, are deployed on a Xilinx Kintex-7 FPGA. Powered by the GRU, the FLI setup can retrieve real-time fluorescence lifetime images at up to 10 frames per second. The proposed FLI system is promising for many important biomedical applications, ranging from biological imaging of fast-moving cells to fluorescence-assisted diagnosis and surgery.

Keywords First keyword · Second keyword · More

Introduction

Fluorescence lifetime imaging (FLI) is an imaging technique based on the differences in the excited state decay rate from a fluorescent sample[1]. Compared with fluorescence intensity imaging, FLI is robust to excitation intensity fluctuations, variable probe concentration, and limited photobleaching. Besides, through the appropriate use of targeted fluorophores, FLI is able to quantitatively measure the parameters of the microenvironment around fluorescent molecules, such as pH, viscosity, and ion concentrations[2, 3]. With these advantages, FLI has wide applications in biological science such as monitoring protein-protein interactions[4], and plays an increasing role in medical and clinical settings such as visualization of tumor margins[5], cancerous tissue detection[1, 6], and computer-assisted robotic surgery[7, 8].

Time-correlated single-photon counting (TCSPC) is popular among FLI systems due to its superiority over other techniques in terms of time resolution, dynamic range, and robustness, which records the arrival time of individual photons at picosecond precision[9, 10, 11]. Figure 1 shows how these systems work. The instrumentation of a typical TCSPC FLI system features a confocal setup, including a single-photon detector, a dedicated TCSPC module for time

arXiv:2306.15599v1 [eess.IV] 27 Jun 2023

tagging, and a PC for lifetime estimation[12, 9]. Such systems are mostly unsuitable for rising clinical applications such as non-invasive monitoring where a miniaturized and fast TCSPC system is desired [13]. Besides, the huge amount of data created by the TCSPC system lays a great burden on data transfer, data storage, and data processing. A powerful PC, sometimes equipped with dedicated GPUs, is required to acquire and process such data. In the last decade, single-photon avalanche diodes (SPADs), solid-state photodetectors sensitive to individual photons, attract increasing attention. Since the successful implementation of SPAD with CMOS technology, SPADs can be massively manufactured at affordable prices, with the potential to be organized into arrays for widefield imaging and coupled with other ICs or FPGAs for in-sensor and near-sensor processing[14, 15, 16].

Least-square (LS) fitting and maximum likelihood estimation (MLE) are widely used for fluorescence lifetime estimation[17, 18, 19]. These two methods rely on iterations to achieve high accuracy, which is time-consuming and computationally expensive. Various non-fitting methods have been proposed to tackle these problems but often compromise on other specifications, among which the Center-of-Mass method (CMM) is a typical one. CMM is a simple, fast, and photon-efficient alternative, which has been already applied in some real-time FLI systems[20, 21, 22]. However, it is very sensitive to background noise, and the estimation is biased due to the use of truncated histograms[23].

Neural networks provide a new path to lifetime determination[24]. The first neural network-based model for fluorescence lifetime estimation was proposed in 2016, where higher accuracy and faster processing than LS fitting were reported[25]. Since then, several neural network architectures, including the fully connected neural network (FCNN), convolutional neural network (CNN), and generative adversarial network (GAN), have been explored for this end[26, 27, 28, 29, 30], which show the ability to resolve multi-exponential decays and achieve accurate and fast estimation even in low photon-count scenarios. Apart from lifetime determination, these neural networks can extract high-level features and be integrated into a large-scale neural network for end-to-end lifetime image analysis such as cancerous tissue margin detection[31] and microglia detection[32].

In this work, we propose to adopt the paradigm of edge artificial intelligence (Edge AI), constructing a recurrent neural network (RNN)-coupled SPAD TCSPC system for real-time FLI. We train and test variants of RNNs for lifetime estimation, and deploy them on FPGA to realize event-driven and near-sensor processing. The working principle is illustrated in Figure 1. Upon the arrival of every photon, the timestamp is processed by the RNN directly without histogramming. From photon detection to lifetime estimation, the whole system is integrated into a miniaturized device, and the system shows a reduced data transfer rate, improving speed, high accuracy, and robustness. With the flexibility to retrain neural networks, the same system can be easily reused for other applications.

Results

Performance of RNNs on Synthetic Dataset

We train and evaluate RNNs on synthetic datasets. Three RNN variants, namely simple RNN, gated recurrent unit (GRU)[33], and long short-term memory (LSTM)[34], are adopted. These RNNs are constructed with 8, 16, and 32 hidden units. LS fitting and CMM are also benchmarked. The metrics used for evaluation are the root mean squared error (RMSE), mean absolute error (MAE), and mean absolute percentage error (MAPE). A common range of lifetime is covered here, which is from 0.2 to 5 ns, and we assume a laser repetition frequency of 20 MHz.

We start with a simple situation in which background noise is absent. All the tests are run on a PC with 32-bit floating point (32FP) precision. The results are presented in Table 1. One can observe that CMM achieves the lowest error in MAE and MAPE, GRU-32 achieves the lowest RMSE error, and GRU-32 and LSTM-32 have very similar performance to CMM. The performance of CMM itself is understandable. In this case, background noise is not considered, and the repetition period is 10 times the longest lifetime. Under these conditions, CMM is very close to the maximum likelihood estimator of the lifetime. When comparing Simple RNN, GRU, and LSTM, one can observe that GRU outperforms LSTM by a small margin, and both of them perform much better than Simple RNN. As we can see with the decrease in model size, errors increase accordingly.

Background noise is often inevitable during fluorescence lifetime imaging, especially in diagnostic and clinical setups where the interruption to existing workflows is supposed to be minimized[13]. In the FLI system that we are going to build, it is estimated that at least 1% of the collected timestamps are from background noise. Therefore, we study the performance of each method under varying background noise levels. For simplicity, only LSTM-32 is used to compare with benchmarks. LSTM-32 is trained on a synthetic dataset, where 0 to 10% uniform background noise is added to samples randomly. Here we also illustrate the result of CMM with background noise subtraction, assuming that the number of photons from background noise is known though it is often not the case in real-time FLI systems. Two synthetic datasets are built for evaluation, where the background noise ratios are 1% (SNR=20dB) and 5% (SNR=12.8dB), respectively. The results are presented in Table 2. We can see that LSTM-32 outperforms other methods

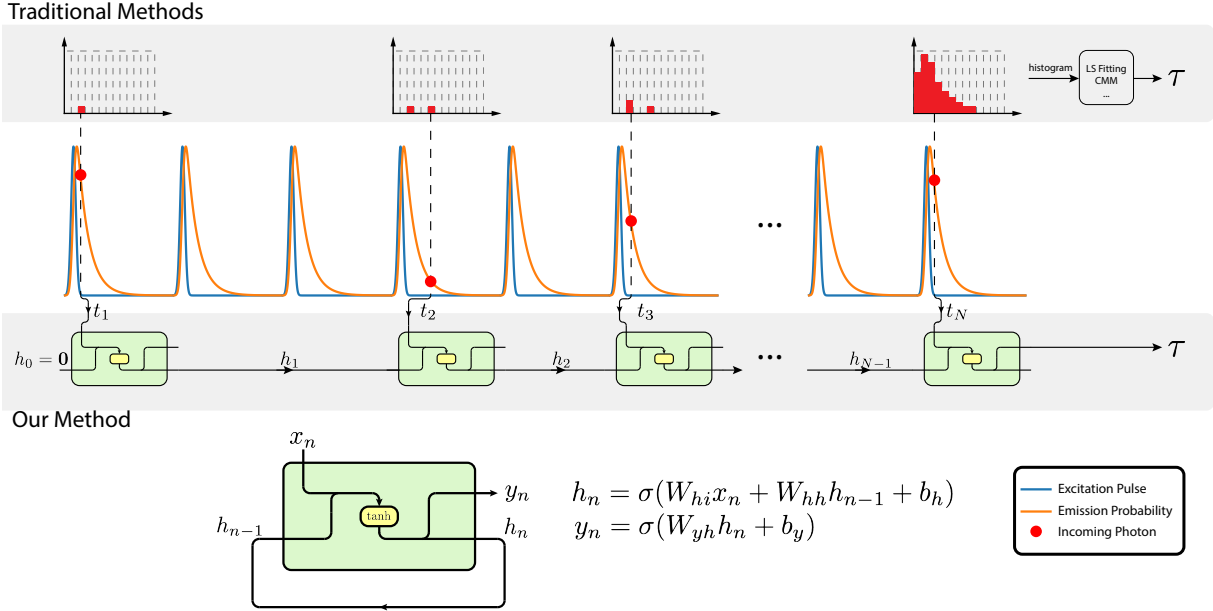


Figure 1: In a traditional TCSPC FLI system, the sample is excited by a laser repeatedly, and the emission photons are detected and time-tagged (Top). A histogram is gradually built on these timestamps, from which the lifetime can be extracted after the acquisition is completed. In our proposed system, upon the receiving of a photon, the timestamp is fed into the RNN immediately (Bottom). The RNN updates the hidden state accordingly and idles for the next photon. The schematic and formula of simple RNN are shown here. At timestep n , the RNN takes the current information x_n and the past information h_{n-1} as input, then updates the memory to the current information h_n and gives out a prediction y_n . σ is the activation function, which is normally tanh for Simple RNN. W and b are the weights and biases.

Model	RMSE	MAE	MAPE
LS Fitting	0.1642	0.1201	0.0553
CMM	0.0915	0.0642	0.0250
Simple RNN-8	0.2516	0.1979	0.0969
Simple RNN-16	0.2396	0.1798	0.0771
Simple RNN-32	0.1877	0.1415	0.0659
GRU-8	0.0957	0.0695	0.0297
GRU-16	0.0928	0.0666	0.0274
GRU-32	0.0908	0.0647	0.0261
LSTM-8	0.0981	0.0720	0.0423
LSTM-16	0.0928	0.0669	0.0277
LSTM-32	0.0916	0.0656	0.0267

Table 1: RNN models are trained and tested on a synthetic dataset, where the fluorescence decay model is mono-exponential, lifetime ranges from 0.2 and 5 ns, laser repetition frequency is 20 MHz, and background noise is not considered. Their performance is benchmarked against Least-square (LS) fitting and Center-of-Mass method (CMM). RMSE: root mean squared error, MAE: mean absolute error, MAPE: mean absolute percentage error.

	1% Background Noise			5% Background Noise		
	RMSE	MAE	MAPE	RMSE	MAE	MAPE
LS fitting	0.1678	0.1226	0.0562	0.1883	0.1368	0.0609
CMM	0.2367	0.2168	0.1577	1.0742	1.0635	0.7799
CMM*	0.1099	0.0839	0.0456	0.2476	0.2128	0.1444
LSTM-32	0.1019	0.0733	0.0304	0.1097	0.0784	0.0323

Table 2: Performance of LS fitting, CMM, CMM with background subtraction, and LSTM-32 in the presence of 1% and 5% background noise. *CMM with background noise subtraction. LSTM-32 is trained on a dataset including 0% to 10% random background noise for generalization in different scenarios.

in all metrics and scenarios. Combined with Table 1, one can observe that errors increase when the background noise increases for all the methods. However, LSTM and LS fitting are more robust to background noise, while CMM is extremely sensitive to it. This finding is in agreement with previous studies[35, 1].

Cramer-Rao Lower Bound Analysis

To compare the performance with the theoretical optima, the Cramer-Rao lower bound (CRLB) is calculated with an open source software [35], given the setting parameters. The variances of the lifetime estimation methods are calculated from Monte Carlo experiments. As for CMM and RNN, 3000 samples are used; as for the least-squares method, 1000 samples are used due to its long running time.

The relationship between lifetime and the relative standard deviation of the different estimators is shown in Figure 2a, where the photon count is 1024. One can observe that the variances of CMM and LSTM-32 almost reach the CRLB, which suggests that CMM and LSTM-32 are almost optimal estimators. Considering that the laser repetition period is much longer than the lifetime and that background noise is not included, it is understandable that CMM reaches the CRLB, since it is approximately an efficient maximum likelihood estimator. LS fitting performs worse than CMM and LSTM-32, which might be due to the underlying assumption of Gaussian errors.

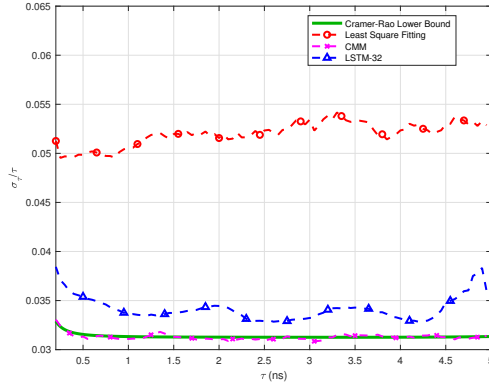
The relationship between the number of photons and the relative standard deviation of the different estimators is shown in Figure 2b, where the lifetime is set at 2.5 ns. Similar to Figure 2a, the relative standard deviations of CMM and LSTM-32 almost reach the CRLB, while the least square fitting performs worse. This result suggests that CMM and LSTM-32 are efficient estimators over different photon inputs, achieving excellent photon efficiency. They only need less than half of the data to obtain similar results as LS fitting.

We also analyze the CRLB with background noise. The results are shown in Figure 3 and Figure 4. Comparing Figure 3a and Figure 4a with Figure 2a, we can see the CRLB is lifted a bit in the presence of background noise. The relative standard deviation of LS fitting stays almost unchanged, and that of LSTM-32 increases slightly but is still much better than LS fitting. As for CMM, one can see that the relative standard deviation increases dramatically at shorter lifetimes, which suggests that CMM is very sensitive to background noise for short lifetimes. By comparing Figure 3b and Figure 4b with Figure 2b, we find that the relative standard deviation almost stays the same in the presence of 1% background noise. With 5% background noise, however, CMM shows a clear degradation of performance, its relative standard deviation getting close to the one of LS fitting.

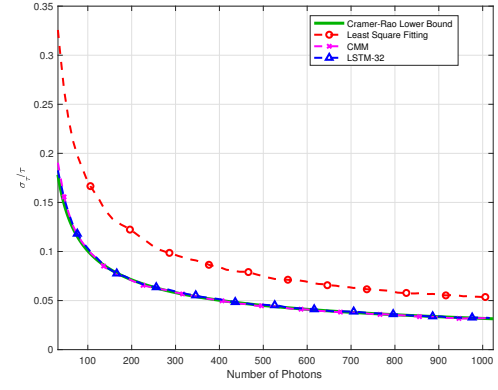
Performance on Experimental Dataset

To verify the performance of RNNs, which are purely trained on synthetic datasets, on real-world data, the RNNs are tested on experimental data along with CMM and LS fitting as benchmarks. We prepare a fluorescence lifetime-encoded microbeads sample and acquire the TCSPC data with a commercial confocal FLIM setup. It is estimated that the background noise is below 1%. The LSTM-32 trained with 0% to 10% background noise dataset is used. The corresponding results are shown in Figure 5.

The histograms of the three samples share a similar shape. As for LS fitting, an instrument response function (IRF) is estimated from histograms of all pixels and then shared among them, which accounts for its good performance here. The result of CMM has a 2 ns bias, which is corrected by the estimated IRF. It is worth noting that for the first peak in the histogram, LSTM shows a sharper Gaussian shape, which confirms LSTM’s good performance under low fluorescence intensity and short lifetime.

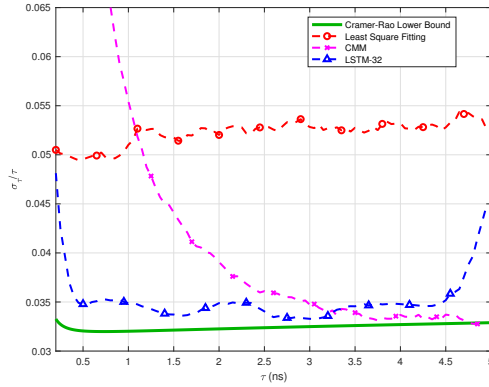


(a) Relative standard deviation of different estimation methods and CRLB as a function of lifetime for a fixed number of detected photons (1024).

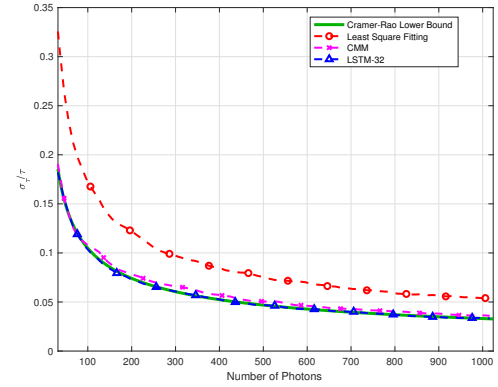


(b) Relative standard deviation of different methods and CRLB as a function of the number of detected photons for a fixed lifetime of 2.5 ns.

Figure 2: Cramer-Rao lower bound analysis.

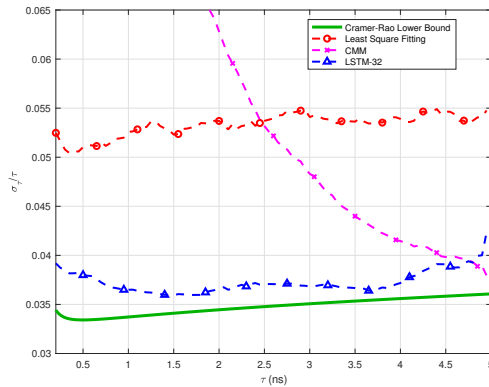


(a) Relative standard deviation of different estimation methods and CRLB as a function of lifetime for a fixed number of detected photons (1024).

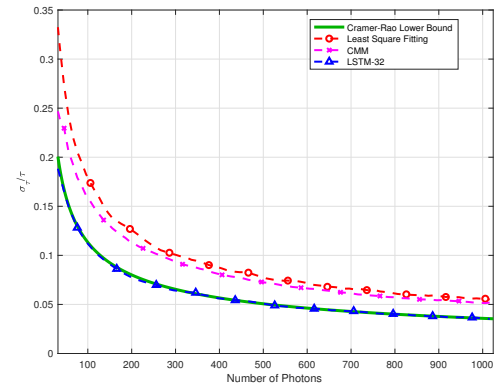


(b) Relative standard deviation of different methods and CRLB as a function of the number of detected photons for a fixed lifetime of 2.5 ns.

Figure 3: Cramer-Rao lower bound analysis when including a 1% background noise level,



(a) Relative standard deviation of different estimation methods and CRLB as a function of lifetime for a fixed number of detected photons (1024).



(b) Relative standard deviation of different methods and CRLB as a function of the number of detected photons for a fixed lifetime of 2.5 ns.

Figure 4: Cramer-Rao lower bound analysis when including a 5% background noise level.

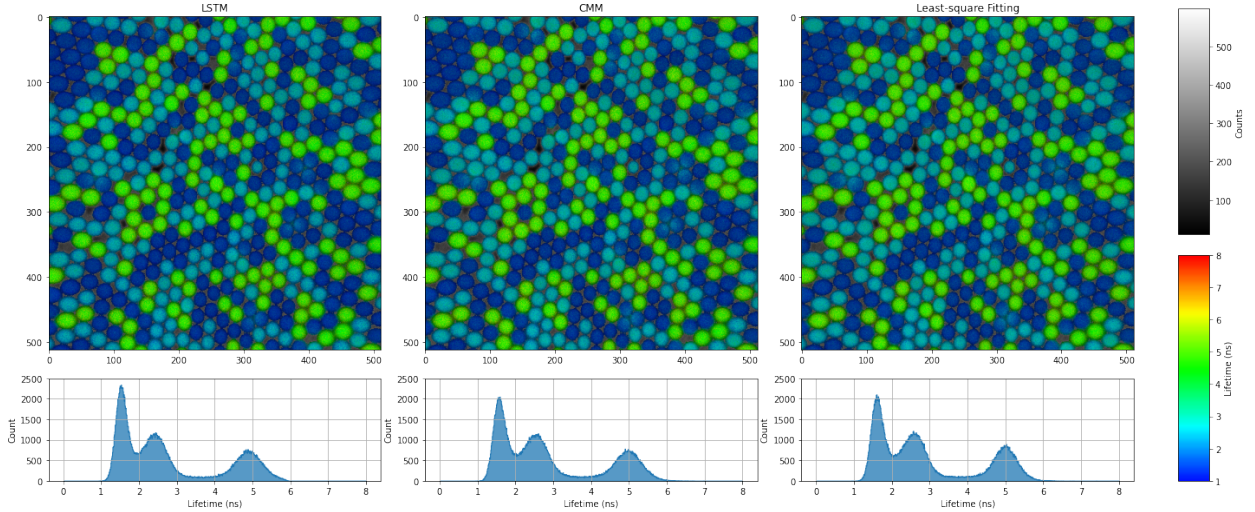


Figure 5: Comparison of LSTM, CMM, and LS Fitting on experimental data. The sample contains a mixture of fluorescent beads with three different lifetimes (1.7, 2.7, and 5.5 ns). The fluorescence lifetime images are displayed using a rainbow scale, where the brightness represents photon counts and the hue represents lifetimes. The lifetime histograms among all pixels are shown below. Most pixels are assumed to contain mono-exponential fluorophores. Two or three lifetimes might be mixed at the edge of the beads.

Real-time FLIM Setup with on-FPGA RNN

We further build a real-time FLIM system by utilizing a SPAD array sensor with on-chip time-to-digital converters (TDCs) and deploying the aforementioned RNNs on FPGA for near-sensor processing. The schematic of our setup is shown in Figure 6. The 32×32 Piccolo SPAD sensor developed at EPFL is utilized, on which 128 TDCs offer 50 ps temporal resolution. The sensor is controlled by a Kintex-7 FPGA, where four GRU cores are implemented for lifetime estimation. The four GRU cores are able to process up to 4 million photons per second. While the data transfer rate to the PC is 20Mb/s for histogram mode and 80Mb/s for raw mode, it reduces to only 240kb/s when applying the proposed RNN-based lifetime estimation method.

We prepare a sample containing fluorescent beads of one lifetime (5.5 ns). The sample is measured by our system in real-time at 5 frames per second. During the imaging, we move the sample plate forward to observe the movement of beads in the images. The result is shown in Figure 7. The lifetime images are also displayed in rainbow scale. The average photon count for the beads is around 500 per pixel. This illustrates that our system can capture well the movement of beads and provide an accurate lifetime estimation. One can also observe that there are some outliers, e.g. dark blue dots and red dots among the green beads. Apart from statistical fluctuations, RNN-based lifetimes tend to be lower when there are not enough photons, which explains why the blue dots are mostly darker than the surrounding pixels.

Discussion

In this work, we present an RNN-coupled SPAD TCSPC system for real-time fluorescence lifetime imaging. The proposed on-FPGA RNN gets rid of the histogramming altogether by taking raw timestamps as input directly, which releases hardware resources on FPGA or PC and significantly reduces the burden on data transfer and data processing. The analysis of synthetic data and CRLB shows that RNN, as a data-driven method, reaches excellent accuracy and robustness compared to its competitors, while retaining higher photon efficiency.

The performance of the system can be further improved by using a larger SPAD sensor and accommodating more RNN cores on the FPGA. A more powerful FPGA or even dedicated neural network accelerators can be used to accommodate more RNN cores. More efficient quantization and approximate schemes can also be explored to reduce resource utilization and latency. Besides, these GRU cores can be further optimized by VHDL implementation. In the future, the RNN cores could be implemented on ASIC and stacked together with SPAD arrays by means of 3-D stacking technology, realizing in-sensor processing[36].

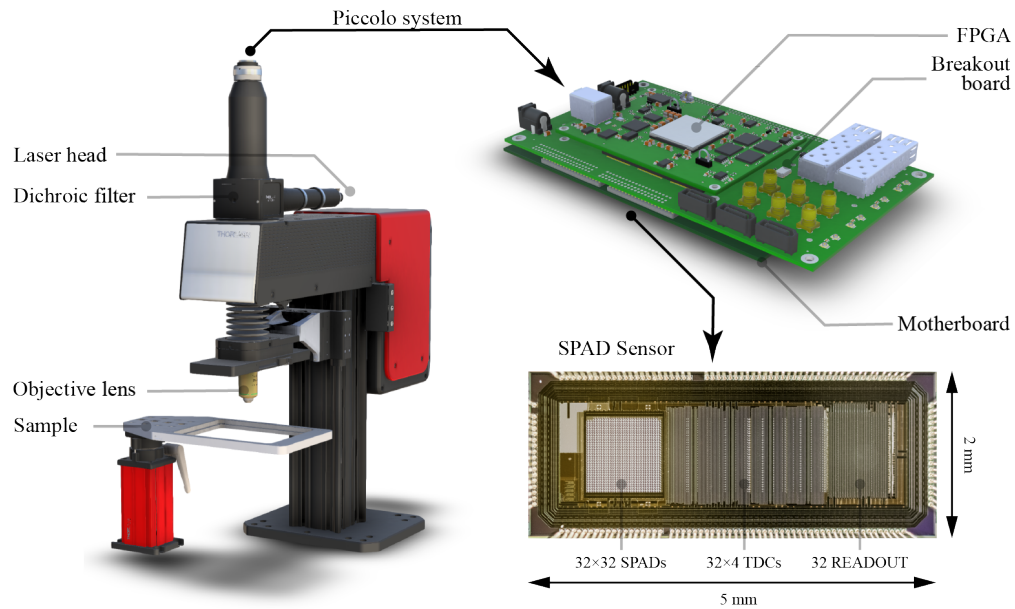


Figure 6: Real-time FLIM system based on the Piccolo 32×32 SPAD sensor and on-FPGA RNNs. The main body of the microscope is from a single-channel Cerna[®] Confocal Microscope System (Thorlabs, Newton, New Jersey, United States). On the top is the Piccolo system, composed of the SPAD sensor itself, motherboard, breakout board, and FPGA. The SPAD sensor has 32×32 SPADs and 128 on-chip TDCs, offering 50 ps temporal resolution. The FPGA is programmed to control the SPAD sensor and communicate with PC through USB 3. The RNN is also deployed on the same FPGA.

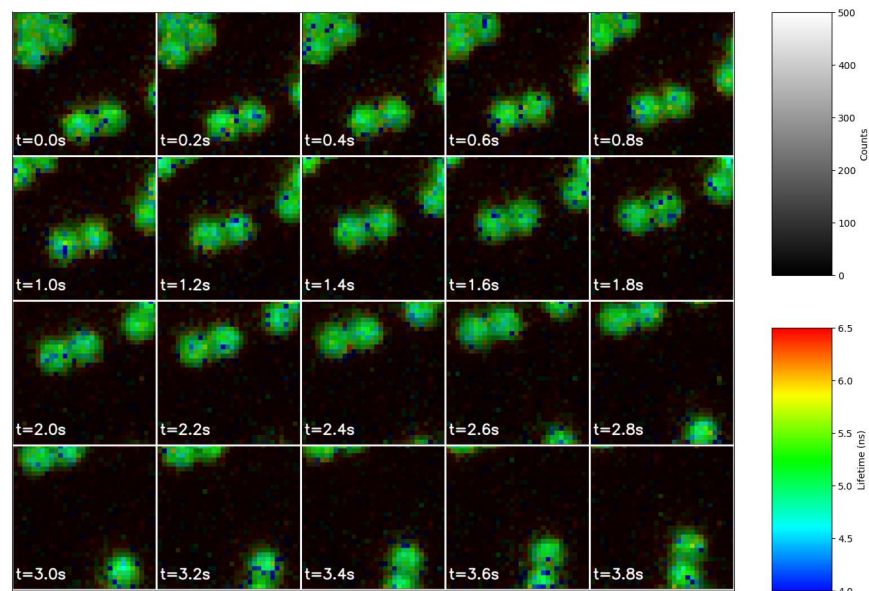


Figure 7: Real-time lifetime image sequence from our FLIM system. The sample contains fluorescent beads with a 5.5 ns reference lifetime.

Though the proposed system is only used for FLI to this date, it can be easily adapted for other applications by retraining the RNN. It can be further combined with other large-scale neural networks for high-level applications, where the output of the RNN is composed of high-level features learned by neural networks automatically, and it serves as input for other neural networks. The existing FLI-based high-level applications such as margin assessment[5, 31] could also be directly incorporated into our system.

Methods

Dataset

Synthetic Dataset

A simulation that well captures the features of the real scene is the key to constructing synthetic datasets. To accurately model a real FLI system, we take fluorescence decay, instrument response, background noise, and dark counts into account. The latter two are often neglected in previous studies. However, in several scenes such as fluorescence-assisted surgery exist strong background noise which can not be simply ignored. Different from existing NN-based methods, which take histograms as input, we generate synthetic datasets on the timestamp level. Assuming that at most one photon reaches the detector in every repetition period (i.e. the pile-up effect is not considered), the timestamps t , namely the arrival time of photons, are modeled as:

$$t = \sum_{i=1}^{N-1} \mathbf{1}_{k=i}(t_{fluoi} + t_{irf}) + \mathbf{1}_{k=N}t_{bg} \quad (1)$$

where $\mathbf{1}$ is the indicator function, k is the component indicator, t_{fluoi} is the fluorescence time delay, t_{irf} is the instrument response time delay, and t_{bg} is the arrival time of background noise or dark counts.

The component indicator k is a random variable with categorical distribution, representing the source of the incoming photon, which can be either a component of the fluorescence decay or background noise. The probability density function (PDF) of k is

$$f(k|\mathbf{p}) = \prod_{i=1}^N p_i^{\mathbf{1}_{k=i}} \quad (2)$$

where p_i represents the normalized intensity of fluorescence or background noise.

The fluorescence time delay t_{fluoi} is subject to an exponential distribution. Its PDF is:

$$f(t_{fluoi}|\tau_i) = \frac{1}{\tau_i} e^{-\frac{t_{fluoi}}{\tau_i}} \quad (3)$$

where τ_i is the lifetime of the fluorescence decay.

The instrument response time delay t_{irf} is subject to a Gaussian distribution. Its PDF is:

$$f(t_{irf}|t_0, \sigma) = \frac{1}{\sqrt{2\pi}\sigma} e^{-\frac{1}{2}\left(\frac{t_{irf}-t_0}{\sigma}\right)^2} \quad (4)$$

where t_0 is the peak position, and σ can be represented by full width at half maximum(FWHM):

$$\sigma = \frac{FWHM}{2\sqrt{2\ln 2}} \quad (5)$$

The time of arrival of background noise t_{bg} is subject to a uniform distribution. Its PDF is:

$$f(t_{bg}|T) = \frac{1}{T} \quad (6)$$

where T is the repetition period.

Given a set of the above parameters, synthetic datasets can be generated with different lifetime ranges, background noise ratios, and components of fluorescence. In this work, the FWHM is assumed to be 167.3 ps, in accordance with previous studies[28, 29]; t_0 for each sample is generated from a uniform distribution from 0 to 5 ns. To train models in the presence of background noise, p_N for each sample is generated from a uniform distribution from 0 to 10%. Each dataset contains 500,000 samples, and each sample contains 1024 timestamps.

Experimental Dataset

Testing the model, which is purely trained on synthetic data, on experimental data is essential to ensure its applicability in real-world scenarios, thus an experimental dataset is curated for evaluation. Fluorescent beads from PolyAn with reference lifetimes of 1.7, 2.7, and 5.5 ns are adopted as the sample. The beads are made of 3D-carboxy, with a diameter of 6.5 μm . The excitation wavelength is around 488 nm and the emission spectra are 602-800 nm, 545-800 nm, and 559-718 nm, respectively. The fluorescence intensity of these three beads is around 1:2:5. Fluorescent beads with different lifetimes are mixed together with all possible combinations, and put in a 384-well plate for imaging.

A commercial FLIM system, available at the Bioimaging and Optics Platform (BIOP) of EPFL, is utilized to measure the sample and acquire the experimental data. A confocal microscope (Leica SP 8, w/ HyD SMD detector) is used for imaging, a super-continuum laser (NKT Photonics, SuperK Extreme EXW-45) is used for illumination, and a TCSPC module (PicoHarp 300 TCSPC) is used for time-tagging. The sample is excited under a 20 MHz laser, corresponding to a repetition period of 50 ns. The excitation wavelength is 486 nm and the spectrum of the emission filter ranges from 600 to 700 nm. The temporal resolution of time-tagging is 16 ps.

Neural Network

The neural network is first built, trained, and evaluated on the PC with PyTorch[37]. Then its weights are quantized and the activation functions are approximated. After that, the neural network is written in C/C++, loading the quantized weights and approximated activation functions, and is further translated into hardware description language (HDL) by Vitis High-level Synthesis (HLS).

Model

Three RNN variants are adopted here, which are simple RNN, GRU, and LSTM. The default models in PyTorch are used. The input size is 1, which is for the timestamps. Considering the hardware limitation, only single-layer RNNs are considered. The hidden sizes range from 8 to 64. Since the timestamps are processed in real-time without storing, bidirectional RNNs cannot be used. An FCNN with one hidden layer takes the hidden state as input to predict the lifetime.

Training

Normally, the loss function for RNNs is built on the output of the last timestep or the average output of all timesteps. In fluorescence lifetime estimation, the performance of estimators is supposed to be improved with more photons. Under this principle, we design a weighted mean square percentage error (MSPE) function, assigning more importance to subsequent timesteps:

$$L(\mathbf{y}, \hat{\mathbf{y}}) = \sum_{i=1}^N w_i \left(\frac{y_i - \hat{y}_i}{y_i} \right)^2 \quad (7)$$

where N is the number of timesteps, \mathbf{y} is the ground truth, $\hat{\mathbf{y}}$ is the prediction, and w_i is the weight at timestep i :

$$w_i = \frac{1}{1 + e^{-\left(\frac{i-N/4}{N/4}\right)}} \quad (8)$$

The weights for hidden states are initialized by an orthogonal matrix. All biases are initialized with 0s. For LSTM, the weights for cell states are initialized by Xavier initialization, and the bias for forget gates is initialized with 1s.

The dataset is randomly split into training, evaluation, and test set, with the ratio of 8:1:1. The batch size is 32. Adam optimizer is used with an initial learning rate of 0.001[38]. The learning rate decays every 5 epochs at the rate of 0.9. The whole training process takes 100 epochs.

Evaluation

Three metrics are used to evaluate the performance of RNNs and benchmarks on synthetic data, which are:

$$\text{RMSE} = \frac{\sqrt{\sum_{i=1}^N (y_i - \hat{y}_i)^2}}{N} \quad (9)$$

$$\text{MAE} = \frac{\sum_{i=1}^N |y_i - \hat{y}_i|}{N} \quad (10)$$

$$\text{MAPE} = \frac{\sum_{i=1}^N \left| \frac{y_i - \hat{y}_i}{y_i} \right|}{N} \quad (11)$$

Cramer-Rao Lower Bound

Cramer-Rao lower bound (CRLB) gives the best precision that can be achieved in the estimation, which has been used in the study of fluorescence lifetime estimation[39, 40, 35]. CRLB expresses a lower bound of variance of estimators, which is proportional to the inverse of Fisher information:

$$\text{Var}(\hat{\theta}) \geq \frac{(f'(x; \theta))^2}{\mathcal{J}(\theta)} \quad (12)$$

where $f(x; \theta)$ is the PDF and \mathcal{J} is the Fisher Information, which is defined as:

$$\mathcal{J}(\theta) = nE_{\theta} \left[\left(\frac{\partial}{\partial \theta} \ln f(x; \theta) \right)^2 \right] \quad (13)$$

The CRLB is calculated with open-source software[35].

FPGA Implementation

Quantization is an effective way to reduce resource utilization and latency on hardware. In common deep learning frameworks such as PyTorch or Tensorflow, model weights and activations are represented by 32-bit floating point numbers. However, it would be inefficient to perform operations for floating point numbers with such bitwidth. We aim to quantize the 32-bit floating point numbers with fixed-point numbers, and reduce the bitwidth as much as possible while maintaining the same model behavior.

Both PyTorch and TensorFlow provide tools of quantization for edge devices, namely PyTorch Quantization and TensorFlow Lite. However, the quantized models rely on their own libraries to run, and the quantized weights cannot be exported. Therefore, we use Python and an open-source fixed point number library to realize a quantized GRU for evaluation. We compare 8-bit, 16-bit, and 32-bit fixed-point numbers to quantize weights and activations separately. The results show that the weights can be quantized to 16-bit fixed point numbers without a significant accuracy drop, and to 8-bit fixed point numbers with an acceptable accuracy drop. Activations can be quantized to 16-bit fixed point numbers without a significant accuracy drop, but 8-bit fixed point quantization will lead the model to collapse. Besides the fixed point precision, we find that the rounding method has a great impact on the performance. Truncating, often the default rounding method, brings larger error. Fixed point numbers with convergent rounding have almost the same behavior as floating point numbers.

The quantized GRU model is then implemented on FPGA. For convenience, the GRU is written in C++ and compiled to Vivado IP with Vitis HLS. The whole model is divided into two parts: a GRU core and an FCNN. The GRU core is designed to be shared among a group of pixels, and the FCNN will be run sequentially for each pixel after integration. Upon receiving a timestamp, GRU core loads hidden states from block RAMs (BRAMs), updates the hidden states, and sends them back to BRAM. After the integration of each repetition period, the FCNN loads the hidden state from BRAM, and streams the estimated lifetime to a FIFO.

Experimental Setup

A real-time FLIM system with our SPAD sensor and on-FPGA RNN is built, which is shown in Figure. 6. The microscope is adapted from the sa confocal microscope system (Single-Channel Cerna Confocal Microscope System), though it is only used for widefield imaging in this work. The same fluorescent bead samples are planned to be measured, hence a 480 nm pulsed laser (PicoQuant) is utilized. A set of filters is adopted for fluorescence imaging. The excitation filter (Thorlabs FITC Excitation Filter) has a central wavelength of 475 nm with a bandwidth of 35 nm. The emission filter is a long-pass filter (Thorlabs Ø25.0 mm Premium Longpass Filter) with a cut-on wavelength of 600 nm. The dichroic filter (Thorlabs GFP Dichroic Filter) has a reflection band from 452 to 490 nm and a transmission band from 505 nm to 800 nm.

A 32 by 32 single-photon avalanche diode (SPAD) sensor with on-chip time-to-digital converters (TDCs) is adopted for single-photon detection and time tagging[41]. The micrograph is also shown in Figure 6. It provides 50 ps temporal resolution and 47.8% peak photon detection probability (PDP). Versions with microlenses are available as well, to

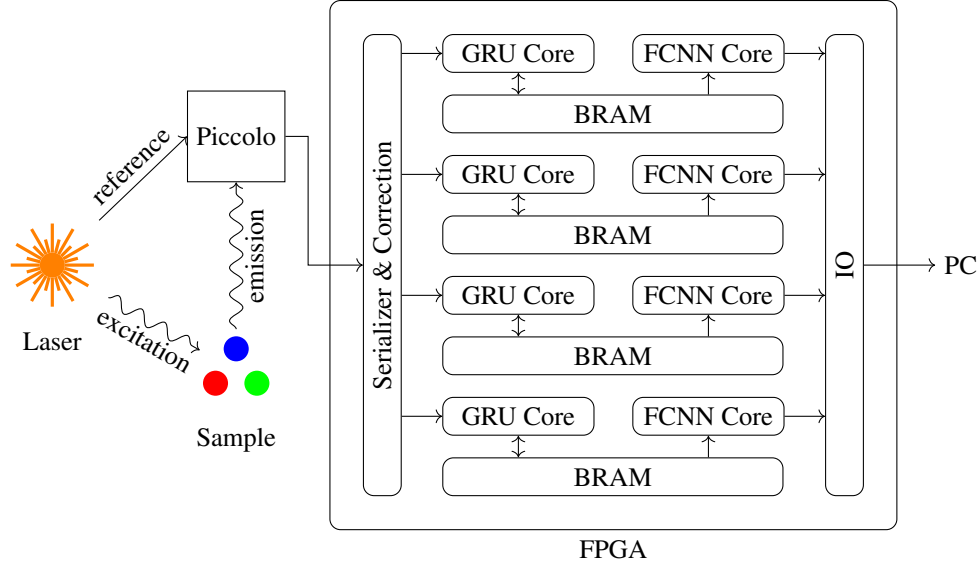


Figure 8: Schematic of the proposed real-time FLIM system with on-FPGA GRUs. A pulsed laser illuminates the sample repeatedly and sends a reference signal to Piccolo to reset TDCs at the same time. The emitted fluorescence photon is then detected by Piccolo and time-tagged, whose arrival time is sent to FPGA in parallel for further processing. The incoming timestamps are serialized and corrected and then sent to GRU cores. The hidden states of GRU are stored in the BRAM. Upon the arrival of a timestamp, the hidden state of the corresponding pixel is read by the GRU core, then the hidden state is updated and written back to the BRAM. After the integration period, the final hidden states are read by FCNN cores and the lifetime is estimated and sent to PC.

improve the light collection efficiency. The median dark count rate (DCR) is 113 cps (per pixel at room temperature). A Xilinx FPGA is used to communicate with the PC and control the sensor. To minimize the system and reduce latency, the RNNs are deployed on the same FPGA.

The schematic of the FPGA design is shown in Figure 8. Four computation units are realized, each of which is in charge of a quarter of the sensor (32 by 8 pixels). The timestamps, sent to FPGA in parallel, are serialized and distributed to four computation units based on their SPAD IDs. Each computation unit is composed of one GRU core, one two-layer fully connected neural network (FCNN) core, and one BRAM. The computation speed is mainly limited by the latency of the GRU core, which is 1.05 ns when employing a 160 MHz clock. The photons that arrive when computation units are busy are simply discarded. The four computation units together are capable of processing up to 4 million photons per second.

References

- [1] Rupsa Datta, Tiffany M. Heaster, Joe T. Sharick, Amani A. Gillette, and Melissa C. Skala. Fluorescence lifetime imaging microscopy: fundamentals and advances in instrumentation, analysis, and applications. *Journal of Biomedical Optics*, 25(7):1–43, 2020.
- [2] Erik B. van Munster and Theodorus W. J. Gadella. Fluorescence Lifetime Imaging Microscopy (FLIM). In *Microscopy Techniques*, pages 143–175. Springer, Berlin, Heidelberg.
- [3] Klaus Suhling, Liisa M. Hirvonen, James A. Levitt, Pei-Hua Chung, Carolyn Tregidgo, Alix Le Marois, Dmitri A. Rusakov, Kaiyu Zheng, Simon Ameer-Beg, Simon Poland, Simao Coelho, Robert Henderson, and Nikola Krstajic. Fluorescence lifetime imaging (FLIM): Basic concepts and some recent developments. *Medical Photonics*, 27:3–40, 2015.
- [4] Horst Wallrabe and Ammasi Periasamy. Imaging protein molecules using FRET and FLIM microscopy. *Current Opinion in Biotechnology*, 16(1):19–27, 2005.
- [5] Jakob Unger, Christoph Hebisch, Jennifer E. Phipps, João L. Lagarto, Hanna Kim, Morgan A. Darrow, Richard J. Bold, and Laura Marcu. Real-time diagnosis and visualization of tumor margins in excised breast specimens using fluorescence lifetime imaging and machine learning. *Biomedical Optics Express*, 11(3):1216–1230, 2020.

- [6] Mikael T. Erkkilä, David Reichert, Johanna Gesperger, Barbara Kiesel, Thomas Roetzer, Petra A. Mercea, Wolfgang Drexler, Angelika Unterhuber, Rainer A. Leitgeb, Adelheid Woehrer, Angelika Rueck, Marco Andreana, and Georg Widhalm. Macroscopic fluorescence-lifetime imaging of NADH and protoporphyrin IX improves the detection and grading of 5-aminolevulinic acid-stained brain tumors. *Scientific Reports*, 10(1):20492, 2020.
- [7] Brent W. Weyers, Mark Marsden, Tianchen Sun, Julien Bec, Arnaud F. Bewley, Regina F. Gandour-Edwards, Michael G. Moore, D. Gregory Farwell, and Laura Marcu. Fluorescence lifetime imaging for intraoperative cancer delineation in transoral robotic surgery. *Translational Biophotonics*, 1(1-2), 2019.
- [8] Jennifer Phipps, Jakob Unger, Regina Gandour-Edwards, Michael G. Moore, Arnaud Bewley, D. Gregory Farwell, and Laura Marcu. Head and Neck Cancer Evaluation via Transoral Robotic Surgery with Augmented Fluorescence Lifetime Imaging. In *Biophotonics Congress: Biomedical Optics Congress 2018 (Microscopy/Translational/Brain/OTS)*, page CTu2B.3, Washington, D.C. OSA.
- [9] Wolfgang Becker. *TCSPC Handbook 9th edn.* 2021.
- [10] W. Becker. Fluorescence lifetime imaging—techniques and applications. *Journal of microscopy*, 247(2):119–136, 2012.
- [11] Liisa M. Hirvonen and Klaus Suhling. Wide-field TCSPC: methods and applications. *Measurement Science and Technology*, 28(1):012003, 2017.
- [12] Peter Kapusta, Michael Wahl, and Rainer Erdmann. *Advanced photon counting: Applications, methods, instrumentation / volume editors, Peter Kapusta, Michael Wahl, Rainer Erdmann ; with contributions by A. Ahlrichs [and fifty others]*, volume 15 of *Springer Series on Fluorescence, 1617-1306*. Springer, Cham, 2015.
- [13] Alba Alfonso-Garcia, Julien Bec, Brent Weyers, Mark Marsden, Xiangnan Zhou, Cai Li, and Laura Marcu. Mesoscopic fluorescence lifetime imaging: Fundamental principles, clinical applications and future directions. *Journal of Biophotonics*, 14(6):e202000472, 2021.
- [14] M. Caccia, L. Nardo, R. Santoro, and D. Schaffhauser. Silicon Photomultipliers and SPAD imagers in biophotonics: Advances and perspectives. *Nuclear Instruments and Methods in Physics Research Section A: Accelerators, Spectrometers, Detectors and Associated Equipment*, 926:101–117, 2019.
- [15] Claudio Bruschini, Harald Homulle, Ivan Michel Antolovic, Samuel Burri, and Edoardo Charbon. Single-photon avalanche diode imagers in biophotonics: review and outlook. *Light: Science and Applications*, 8(1):87, 2019.
- [16] Iris Cusini, Davide Berretta, Enrico Conca, Alfonso Incoronato, Francesca Madonini, Arianna Adelaide Maurina, Chiara Nonne, Simone Riccardo, and Federica Villa. Historical Perspectives, State of Art and Research Trends of SPAD Arrays and Their Applications (Part II: SPAD Arrays). *Frontiers in Physics*, 10:606, 2022.
- [17] A. Grinvald and I. Z. Steinberg. On the analysis of fluorescence decay kinetics by the method of least-squares. *Analytical Biochemistry*, 59(2):583–598, 1974.
- [18] ?eljko Bajzer, Terry M. Therneau, Joseph C. Sharp, and Franklin G. Prendergast. Maximum likelihood method for the analysis of time-resolved fluorescence decay curves. *European Biophysics Journal*, 20(5):247–262, 1991.
- [19] A. Chessel, F. Waharte, J. Salamero, and C. Kervrann. A Maximum Likelihood method for lifetime estimation in photon counting-based Fluorescence Lifetime Imaging Microscopy. In *21st European Signal Processing Conference (EUSIPCO 2013)*, pages 1–5, 2013.
- [20] I. Isenberg and R. D. Dyson. The analysis of fluorescence decay by a method of moments. *Biophysical Journal*, 9(11):1337–1350, 1969.
- [21] Day-Uei Li, Jochen Arlt, Justin Richardson, Richard Walker, Alex Buts, David Stoppa, Edoardo Charbon, and Robert Henderson. Real-time fluorescence lifetime imaging system with a 32×32 $0.13 \mu\text{m}$ CMOS low dark-count single-photon avalanche diode array. *Optics Express*, 18(10):10257–10269, 2010.
- [22] David D-U Li, Jochen Arlt, David Tyndall, Richard Walker, Justin Richardson, David Stoppa, Edoardo Charbon, and Robert K. Henderson. Video-rate fluorescence lifetime imaging camera with CMOS single-photon avalanche diode arrays and high-speed imaging algorithm. *Journal of Biomedical Optics*, 16(9):096012, 2011.
- [23] Xiongbo Liu, Danying Lin, Wolfgang Becker, Jingjing Niu, Bin Yu, Liwei Liu, and Junle Qu. Fast fluorescence lifetime imaging techniques: A review on challenge and development. *Journal of Innovative Optical Health Sciences*, 12(05):1930003, 2019.
- [24] Varun Mannam, Yide Zhang, Xiaotong Yuan, Cara Ravasio, and Scott S. Howard. Machine learning for faster and smarter fluorescence lifetime imaging microscopy. *Journal of Physics: Photonics*, 2(4):042005, 2020.
- [25] Gang Wu, Thomas Nowotny, Yongliang Zhang, Hong-Qi Yu, and David Day-Uei Li. Artificial neural network approaches for fluorescence lifetime imaging techniques. *Optics Letters*, 41(11):2561–2564, 2016.

- [26] Jason T. Smith, Ruoyang Yao, Nattawut Sinsuebphon, Alena Rudkouskaya, Nathan Un, Joseph Mazurkiewicz, Margarida Barroso, Pingkun Yan, and Xavier Intes. Fast fit-free analysis of fluorescence lifetime imaging via deep learning. *Proceedings of the National Academy of Sciences*, 116(48):24019–24030, 2019.
- [27] Vytautas Zickus, Ming-Lo Wu, Kazuhiro Morimoto, Valentin Kapitany, Areeba Fatima, Alex Turpin, Robert Insall, Jamie Whitelaw, Laura Machesky, Claudio Bruschini, Daniele Faccio, and Edoardo Charbon. Fluorescence lifetime imaging with a megapixel SPAD camera and neural network lifetime estimation. *Scientific Reports*, 10(1):20986, 2020.
- [28] Dong Xiao, Yu Chen, and David Day-Uei Li. One-Dimensional Deep Learning Architecture for Fast Fluorescence Lifetime Imaging. *IEEE Journal of Selected Topics in Quantum Electronics*, 27(4):1–10, 2021.
- [29] Zhenya Zang, Dong Xiao, Quan Wang, Zinuo Li, Wujun Xie, Yu Chen, and David Day Uei Li. Fast fluorescence lifetime imaging analysis via extreme learning machine. *arXiv preprint arXiv:2203.13754*, 2022.
- [30] Yuan-I Chen, Yin-Jui Chang, Shih-Chu Liao, Trung Duc Nguyen, Jianchen Yang, Yu-An Kuo, Soonwoo Hong, Yen-Liang Liu, H. Grady Rylander, Samantha R. Santacruz, Thomas E. Yankeelov, and Hsin-Chih Yeh. Generative adversarial network enables rapid and robust fluorescence lifetime image analysis in live cells. *Communications Biology*, 5(1):18, 2022.
- [31] Mark Marsden, Brent W. Weyers, Julien Bec, Tianchen Sun, Regina F. Gandour-Edwards, Andrew C. Birkeland, Marianne Abouyared, Arnaud F. Bewley, D. Gregory Farwell, and Laura Marcu. Intraoperative Margin Assessment in Oral and Oropharyngeal Cancer Using Label-Free Fluorescence Lifetime Imaging and Machine Learning. *IEEE transactions on bio-medical engineering*, 68(3):857–868, 2021.
- [32] Md Abdul Kader Sagar, Kevin P. Cheng, Jonathan N. Ouellette, Justin C. Williams, Jyoti J. Watters, and Kevin W. Eliceiri. Machine Learning Methods for Fluorescence Lifetime Imaging (FLIM) Based Label-Free Detection of Microglia. *Frontiers in Neuroscience*, 14:931, 2020.
- [33] Kyunghyun Cho, Bart Van Merriënboer, Caglar Gulcehre, Dzmitry Bahdanau, Fethi Bougares, Holger Schwenk, and Yoshua Bengio. Learning phrase representations using RNN encoder-decoder for statistical machine translation. *arXiv preprint arXiv:1406.1078*, 2014.
- [34] Sepp Hochreiter and Jürgen Schmidhuber. Long short-term memory. *Neural computation*, 9(8):1735–1780, 1997.
- [35] Dorian Bouchet, Valentina Krachmalnicoff, and Ignacio Izeddin. Cramér-Rao analysis of lifetime estimations in time-resolved fluorescence microscopy. *Optics Express*, 27(15):21239–21252, 2019.
- [36] Edoardo Charbon, Claudio Bruschini, and Myung-Jae Lee. 3D-Stacked CMOS SPAD Image Sensors: Technology and Applications. In *2018 25th IEEE International Conference on Electronics, Circuits and Systems (ICECS)*, pages 1–4. IEEE, 12/9/2018 - 12/12/2018.
- [37] Adam Paszke, Sam Gross, Francisco Massa, Adam Lerer, James Bradbury, Gregory Chanan, Trevor Killeen, Zeming Lin, Natalia Gimelshein, Luca Antiga, et al. Pytorch: An imperative style, high-performance deep learning library. *Advances in Neural Information Processing Systems*, 32, 2019.
- [38] Diederik P Kingma and Jimmy Ba. Adam: A method for stochastic optimization. *arXiv preprint arXiv:1412.6980*, 2014.
- [39] Malte Köllner and Jürgen Wolfrum. How many photons are necessary for fluorescence-lifetime measurements? *Chemical Physics Letters*, 200(1-2):199–204, 1992.
- [40] Jeongtae Kim and Jiyeong Seok. Statistical properties of amplitude and decay parameter estimators for fluorescence lifetime imaging. *Optics Express*, 21(5):6061–6075, 2013.
- [41] Chao Zhang, Scott Lindner, Ivan Michel Antolovic, Martin Wolf, and Edoardo Charbon. A CMOS SPAD Imager with Collision Detection and 128 Dynamically Reallocating TDCs for Single-Photon Counting and 3D Time-of-Flight Imaging. *Sensors (Basel, Switzerland)*, 18(11):4016, 2018.